Journal of Alloys and Compounds 806 (2019) 1509–1516

Contents lists available at ScienceDirect

Journal of Alloys and Compounds

journal homepage: http://www.elsevier.com/locate/jalcom

Magnetic frustration in partially ordered double perovskites $Ln_3Ni_2RuO_9$ (Ln = La, Nd)

S. Laha [a], J. Gopalakrishnan [a], S. Natarajan [a], J. Romero de Paz [b], E. Solana-Madruga [c], A.J. Dos Santos-García [d], S. García-Martín [c], O. Fabelo [e], E. Morán-Miguélez [c, *], R. Sáez-Puche [c]

[a] Solid State and Structural Chemistry Unit, Indian Institute of Science, Bangalore, 560 012, India
[b] CAI Técnicas Físicas, Facultad de Ciencias Físicas, Universidad Complutense de Madrid, Avda. Complutense s/n, 28040, Madrid, Spain
[c] Departamento de Químicas Inorgánica, Facultad de Ciencias Químicas, Universidad Complutense de Madrid, 28040, Madrid, Spain
[d] Dpto. Ingeniería Química y Diseño Industrial, Universidad Politécnica de Madrid, C/ Ronda de Valencia 3, 28012, Madrid, Spain
[e] Institut Laue Langevin, 71 Avenue des Martyrs, 38042 Grenoble Cedex 9, France

ARTICLE INFO

Article history:
Received 13 March 2019
Received in revised form
7 June 2019
Accepted 29 July 2019
Available online 30 July 2019

Keywords:
Oxide materials
Double perovskite
Solid state metathesis
Powder neutron diffraction
Spin-glass behavior

ABSTRACT

$Ln_3Ni_2RuO_9$ (Ln = La, Nd) oxides (prepared by a solid state metathesis route) adopt a monoclinic ($P2_1/n$) $A_2BB'O_6$ double perovskite structure wherein the two independent octahedral 2c and 2d sites are occupied by Ni^{2+} and ($Ni^{2+}_{1/3}Ru^{5+}_{2/3}$) cations, respectively. In contrast to the expected ferromagnetic behavior, $Ln_3Ni_2RuO_9$ oxides show a spin-glass behavior without long range magnetic order down to 2 K. These results reveal the importance of competing nearest neighbor (NN), next nearest neighbor (NNN) and third nearest neighbor (third NN) interactions between the magnetic Ni^{2+} and Ru^{5+} ions in the partially ordered double perovskite structure that conspire to thwart the expected ferromagnetic order in these materials.

1. Introduction

The versatility of the perovskite structure (ABO_3) [1] to accommodate multiple substitutions at the B site gives rise to a large number of derivatives of general formulas such as $A_2BB'O_6$ and $A_3BB'_2O_9$. The B and B′ cations in these oxides could be long range ordered, resulting in several superstructures and novel electronic properties related thereto [2,3]. The properties of these perovskites depend on the electronic configuration of the A, B and B′ cations. Typical examples of $A_2BB'O_6$ oxides are Sr_2FeMoO_6 (half-metallic ferromagnet) [4], La_2NiMnO_6 (near-room temperature ferromagnetic semiconductor) and Ba_2BiBiO_6 (a charge disproportionated double perovskite that becomes superconducting on Pb substitution) [5–7]. In search of new magnetoelectric materials, several related double perovskites Ln_2MMnO_6 (Ln = La = La, Sm, Gd, Dy and Lu, M = Co, Ni, Fe and Cu) have been investigated in detail in recent times [8–14]. Similarly, oxides of $A_3BB'_2O_9$ formula form ordered (1:2) superstructures, for instance $Ba_3ZnTa_2O_9$, that finds applications in microwave telecommunication devices as dielectric ceramic [15]. Partially ordered $A_3BB'_2O_9$ oxides are also known to display novel electronic properties. For example, $Pb_3MgNb_2O_9$ has a partially ordered structure consisting of Nb and ($Nb_{1/3}Mg_{2/3}$) 1:1 ordering in the $A_2BB'O_6$ double perovskite structure; this material is a well-known relaxor ferroelectric owing to the partial order/disorder [16]. $La_3Ni_2SbO_9$ is a relaxor - ferromagnet that also possesses a 1:1 partially ordered $A_2BB'O_6$ structure, where octahedral B and B′ sites are occupied by Ni and disordered ($Ni_{1/3}Sb_{2/3}$) atoms respectively [17]. Several triclinic, monoclinic, tetragonal and hexagonal perovskite oxides such as $LaSr_2Cr_2SbO_9$ [18], $La_3Ni_2B'O_9$ (B' = Nb, Ta) [19,20], $SrLa_2FeCoSbO_9$ [21], $Sr_3Fe_2TeO_9$ [22], $Sr_3Fe_2WO_9$ and $Ba_3Fe_2WO_9$ [23] have been explored in this direction. Recently, a spin-glass like behavior has been observed in $Sr_3NiSb_2O_9$ [24].

Some years ago, we developed a metathesis route for the synthesis of ABO_3 and $A_2BB'O_6$ perovskite oxides starting from Li-containing rock-salt oxides and appropriate metal chloride/

* Corresponding author.
E-mail address: emoran@ucm.es (E. Morán-Miguélez).

https://doi.org/10.1016/j.jallcom.2019.07.354
0925-8388/

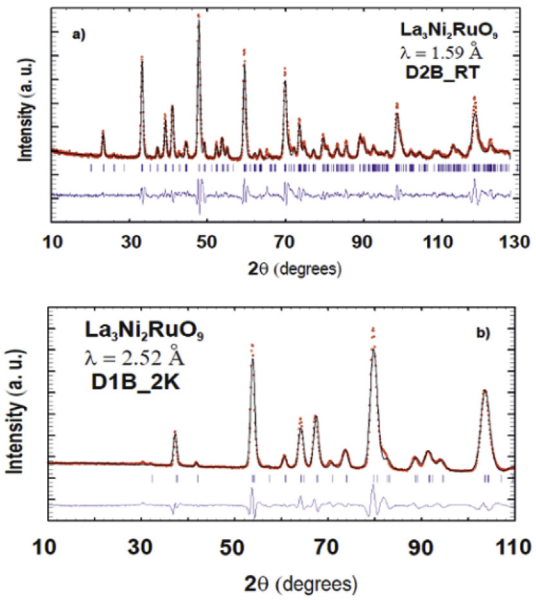

Fig. 1. Rietveld refinement of PND patterns obtained for $La_3Ni_2RuO_9$ at room temperature (a) and 2 K(b). Observed (red dot), calculated (black line), and difference (bottom line) profiles are shown. The vertical bars indicate Bragg reflections (|). (For interpretation of the references to colour in this figure legend, the reader is referred to the Web version of this article.)

oxychloride [25,26]. We have extended this route now for the synthesis of new $A_3BB'_2O_9$ oxides of the formula $Ln_3Ni_2RuO_9$ (Ln = La, Nd), starting from $Li_3Ni_2RuO_6$ rock salt oxides [27] and LnOCl (Ln = La, Nd). We determined the crystal structures of the new nickel-perovskite oxides through powder X-ray diffraction (PXRD), powder neutron diffraction (PND), selected area electron diffraction (SAED) and high resolution transmission electron microscopy (HRTEM), and we have investigated their magnetic properties. The results, reported herein, reveal competing magnetic interactions between Ni^{2+} and Ru^{5+} in the partially ordered double perovskite structure, that preclude a magnetic ordering down to 2K.

2. Experimental section

2.1. Synthesis

$Ln_3Ni_2RuO_9$ (Ln = La, Nd) double perovskites were prepared by the following solid state metathesis reaction:

$$Li_3Ni_2RuO_6 + 3LnOCl \rightarrow Ln_3Ni_2RuO_9 + 3LiCl \uparrow \quad (1)$$

The precursor materials were prepared by conventional ceramic method. Stoichiometric quantities of Li_2CO_3, RuO_2 and $NiC_2O_4 \cdot 2H_2O$ were reacted at elevated temperatures for several hours with intermittent grindings to obtain single phase $Li_3Ni_2RuO_6$ [27]. LnOCl (Ln = La, Nd) were synthesized by reacting Ln_2O_3 (pre-dried overnight at 900 °C) with an equal quantity of NH_4Cl at 300, 500 and 900 °C for 2–4h at each temperature [28]. The metathesis synthesis according to reaction (1) was carried out by heating stoichiometric mixture of the reactants at progressively increasing temperatures up to 1200 °C in air, with intermittent grinding and pelletizing until the formation of single phase product. The LiCl, formed as product, volatilized at the reaction condition (Energy dispersive X-ray spectroscopy -EDS- did not indicate the presence of chloride ions).

2.2. Structural and magnetic characterization

Preliminary PXRD patterns were recorded in the 2θ range 5–80° by means of a PANalytical X'pert Diffractometer operating at 45 kV and 30 mA using Ni-filtered CuKα radiation (λ = 1.542 Å). PXRD data for Rietveld refinement were recorded employing the same instrument in the 2θ range 10–100°, with step size 0.02° and step

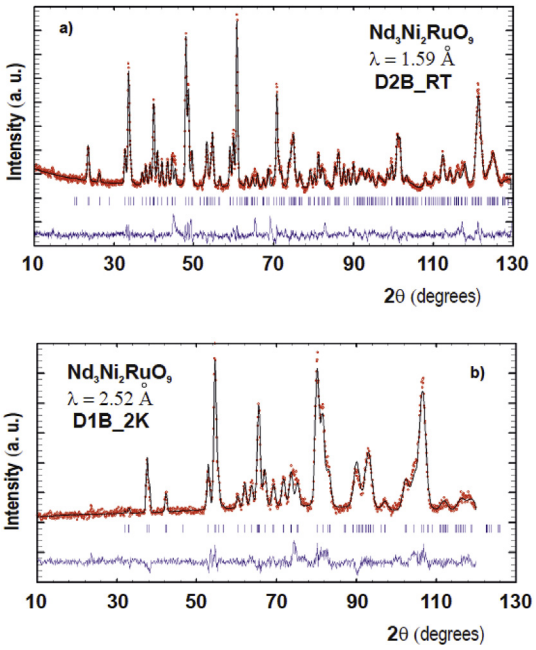

Fig. 2. Rietveld refinement of PND patterns obtained for $Nd_3Ni_2RuO_9$ at room temperature (a) and 2 K(b). Observed (red dot), calculated (black line), and difference (bottom line) profiles are shown. The vertical bars indicate Bragg reflections (|). (For interpretation of the references to colour in this figure legend, the reader is referred to the Web version of this article.)

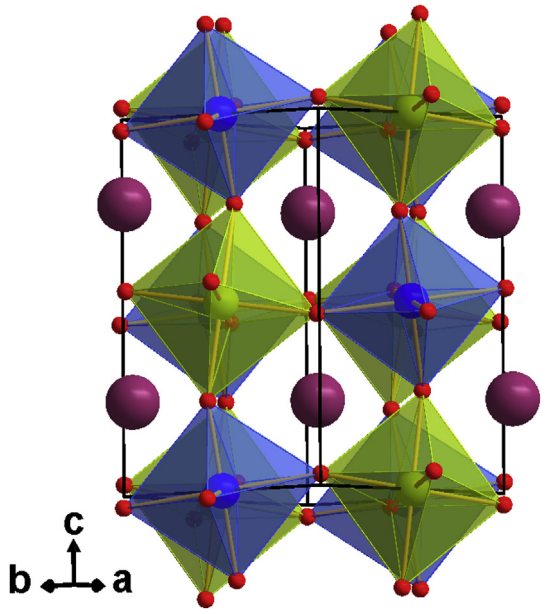

Fig. 3. Crystal structure of $Ln_3Ni_2RuO_9$ (Ln = La, Nd). Blue and green octahedra represent the [Ni(2*c*)O_6] and [Ru/Ni(2*d*)O_6] units, respectively. Large magenta circles are the Ln atoms and small red circles are the oxygens. (For interpretation of the references to colour in this figure legend, the reader is referred to the Web version of this article.)

duration of 50s.

PND data were collected at 300 K on the high resolution D2B diffractometer and at 1.5 K using the high intensity diffractometer D1B, both at the Institute Laue - Langevin (Grenoble, France). 2 g of each sample were placed in sealed vanadium cans within a He-cryostat. The diffraction profiles were collected at D2B in the range $2\theta = 0–130^\circ$ with a neutron wavelength of 1.594 Å and a step-width of 0.05°; the patterns collected at D1B were measured between $2\theta = 0–120^\circ$ with a step-width of 0.1° and a neutron wave length of 2.52 Å. The temperature dependence of $Nd_3Ni_2RuO_9$ magnetic reflections was checked between 1.5 K and 190 K on the D1B diffractometer. PXRD data for $Ln_3Ni_2RuO_9$ was refined by means of GSAS [29]. Combined Rietveld analysis of the PND and PXRD data were carried out using the Fullprof Suite program [30]. PXRD patterns were simulated using the program POWDERCELL [31].

SAED and HRTEM studies were performed with a JEOL JEM 3000F microscope operating at 300 kV (double tilt (±20°) point resolution 1.7 Å), fitted with an EDS microanalysis system (OXFORD INCA). The samples were ground in *n*-butyl alcohol and ultrasonically dispersed. A few drops of the resulting suspension were deposited in a carbon-coated grid. The atomic ratio of the metals was determined through EDS analyses finding a good agreement between analytical and nominal compositions in all the crystals.

Magnetization (M) measurements were performed in a Quantum Design XL Squid magnetometer. The dc magnetic susceptibility (χ) was obtained from dc-M measured in the temperature range 2–300 K at 10 mT, after cooling the sample from room temperature to 2K in a zero field (ZFC) and also after cooling in the measuring field (FC). The real and imaginary components of ac magnetic susceptibility (χ' and χ'' respectively) were obtained from ac-M measured in the temperature range 2–50 K applying an oscillating magnetic field with drive amplitude of 0.35 mT at different frequencies. The magnetic field dependence of dc-M was measured at different temperatures in magnetic field strengths up to 5T. The diamagnetic contribution was subtracted from the calculated molar magnetic susceptibilities [32].

3. Results and discussion

3.1. Structural characterization

$Ln_3Ni_2RuO_9$ (Ln = La, Nd) oxides are readily synthesized by metathesis reaction from $Li_3Ni_2RuO_6$ and LnOCl compounds (1).

Table 1
Structural details for $Ln_3Ni_2RuO_9$ oxides determined from the combined Rietveld refinements of the PND (D2B, room temperature) and PXRD data for Ln = La and Nd.

$P2_1/n$			$La_3Ni_2RuO_9$	$Nd_3Ni_2RuO_9$
Parameter			PND-XRD	PND-XRD
a (Å)			5.5702 (3)	5.4299 (2)
b (Å)			5.5812 (3)	5.6430 (2)
c (Å)			7.8449 (3)	7.7323 (3)
β (deg)			89.660 (3)	90.02 (2)
R_B			6.78	7.53
R_F			4.23	5.20
R_{wp}			9.92	4.41
R_p			7.52	4.67
Atom	**site**			
La/Nd	4e	*x*	0.4863 (4)	0.512 (1)
		y	0.4654 (3)	0.5583 (5)
		z	0.250 (1)	0.248 (2)
		$U_{iso}(Å^2)$	0.15 (3)	0.41 (8)
Ni1/Ru	2d			
(0.33/0.67)	(½ 0 0)	$U_{iso}(Å^2)$	0.30 (5)	0.34 (7)
Ni2	2c (0 ½ 0)	$U_{iso}(Å^2)$	0.30 (5)	0.34 (7)
O1	4e	*X y*	0.776 (3)	0.197 (4)
		z	0.793 (3)	0.190 (3)
			−0.042 (2)	−0.041 (3)
		$U_{iso}(Å^2)$	0.07 (8)	0.59 (7)
O2	4e	*x*	0.701 (3)	0.303 (4)
		y	0.298 (4)	0.705 (3)
		z	−0.034 (2)	−0.051 (3)
		$U_{iso}(Å^2)$	0.07 (8)	0.59 (7)
O3	4e	*x*	0.567 (2)	0.406 (1)
		y	0.008 (2)	0.979 (1)
		z	0.263 (2)	0.248 (4)
		$U_{iso}(Å^2)$	0.07 (8)	0.59 (7)
M	**site**		d (M – O) (Å)	d (M – O) (Å)
Ni1/Ru	2d		2.09 (2) x 2	2.00 (1) x 2
			2.02 (2) x 2	1.97 (2) x 2
			1.95 (2) x 2	1.95 (2) x 2
		$\Delta[MO_6]$	$1.44*10^{-3}$	$4.4*10^{-5}$
Ni2	2c		2.08 (2) x 2	1.99 (3) x 4
			2.03 (2) x 2	2.02 (2) x 2
			1.90 (2) x 2	
		$\Delta[MO_6]$	$1.26*10^{-3}$	$1.45*10^{-4}$
< M-*O*-M> (°)				
<Ni1/Ru–*O*–Ni2>			O1 = 155.6 (4)	O1 = 148.9 (5)
			O2 = 148.3 (4)	O2 = 148.6 (5)
			O3 = 153.3 (4)	O3 = 149.6 (2)

PXRD patterns reveal the formation of single-phase perovskite-type products (Fig. S1). Preliminary Rietveld refinements of the crystal structure from PXRD data (Fig. S2 and Fig. S3), carried out on the basis of $La_3Ni_2SbO_9$ structure model [17], show that both the $Ln_3Ni_2RuO_9$ (Ln = La, Nd) oxides adopt the monoclinic ($P2_1/n$) $A_2BB'O_6$ double perovskite structure with lattice parameters ~ $\sqrt{2}a_p \times$ ~ $\sqrt{2}a_p \times 2a_p$, (where a_p is the cubic perovskite lattice parameter) closely similar to that of $La_3Ni_2SbO_9$, wherein the two independent octahedral sites (2c) and (2d) are occupied by Ni and ($Ni_{1/3}Ru_{2/3}$), respectively. These initial refinements were taken as starting model for the combined PND and PXRD Rietveld refinements. PND data, collected at room temperature in the high resolution D2B diffractometer, account for an accurate determination of the oxygen positions meanwhile PXRD data do it for the B-site cation ordering since neutron scattering lengths for Ru and Ni (7.03 and 10.3 fm respectively) do not allow to confirm the rock-salt ordering at the B-site. Fig. 1(a) and Fig. 2(a) show the results for the Rietveld refinements of the crystal structure from PND data collected at room temperature for $La_3Ni_2RuO_9$ and $Nd_3Ni_2RuO_9$ respectively. Furthermore, the refinement of PND data collected at low temperatures in D1B diffractometer showed that the structure is retained down to 2K (see Figs. 1(b) and Fig. 2(b)). Fig. 3 depicts the crystal structure of $Ln_3Ni_2RuO_9$ (Ln = La, Nd) compounds and Table 1 list the structural details obtained for both compounds at room temperature. The lattice parameters show the expected lanthanide contraction. Bond lengths and angles obtained from the Rietveld refinements indicate that both [NiO_6] and [Ni/RuO_6] octahedra at 2c and 2d sites are almost regular (Table 1) and the lanthanide atoms at 4e sites have an 8-fold oxygen coordination as in other double perovskites with rock salt type ordering [2,3]. The Rietveld refinements reveal no additional ordering between Ni and Ru atoms within the 2d position. This atomic distribution and the long range ordering of the particles were confirmed by SAED and HRTEM, as discussed below. The <Ni–O–Ru/Ni> angles clearly deviate in both compounds (see Table 1) from the 180° ideal value, inducing high tilt angles according to those commonly observed among $A_2BB'O_6$ double perovskites crystallizing in the monoclinic $P2_1/n$ space group. It is worth noting that the PND patterns collected at 2K do not show additional reflections with respect to those collected at room temperature, evidencing the absence of any long-range magnetic order in these compounds. Consequently, low temperature diffraction patterns were easily fitted to the nuclear structural model obtained from room temperature data.

Fig. 4 (a, b and c) depicts SAED patterns along three different zone axes of a crystal of $Nd_3Ni_2RuO_9$. The La-compound presents similar results. The patterns have been indexed according to the cubic perovskite structure and show Bragg reflections characteristic of the perovskite structure and extra reflections at $G_p \pm ½(110)^*_p$, $G_p \pm ½(001)^*_p$ and $G_p \pm ½(111)^*_p$. The reflections at $G_p \pm ½(110)^*_p$ and $G_p \pm ½(001)^*_p$ do not appear in the SAED pattern of the $[-110]_p$ zone axis because they are due to multiple diffraction. Construction of the reciprocal lattice from SAED along different zone axis indicates that the $Ln_3Ni_2RuO_9$ (Ln = La, Nd) oxides have a crystal structure related to perovskite structure with $\sqrt{2}a_p \times \sqrt{2}a_p \times 2a_p$ unit cell. Fig. 4 (d and e) shows the HRTEM images and the corresponding Fast Fourier Transformation (FFT) of the $[-110]_p$ and $[11-1]_p$ zone axes. The HRTEM image of the $[-110]_p$ zone axis shows contrast differences indicating a periodicity corresponding to $2a_p$ along the $[001]_p$ direction and $\sqrt{2}a_p$ along the $[110]_p$ direction and the HRTEM image of the $[11-1]_p$ zone axis presents contrast differences corresponding to a $\sqrt{2}a_p$ periodicity along the $[-110]_p$ direction. The existence of the significantly strong $G_p \pm ½(111)^*_p$ reflection in combination with these contrast differences can be ascribed to the ordering of the B cations. Similar SAED patterns and periodicities deduced from contrast differences in HRTEM images are found in perovskite-systems with rock-salt-type ordering of the B cations [33,34]. Therefore, these SAED and HRTEM results in Fig. 4 indicate that the B cations are distributed within two positions B and B' (2c and 2d) in a rock-salt type ordering in both $La_3Ni_2RuO_9$ and $Nd_3Ni_2RuO_9$ oxides. Additional ordering in one of the two positions (2d), which would originated a larger periodicity, is not observed even in short-range or domains of the crystals. These results are consistent with the structure obtained from PXRD and PND data.

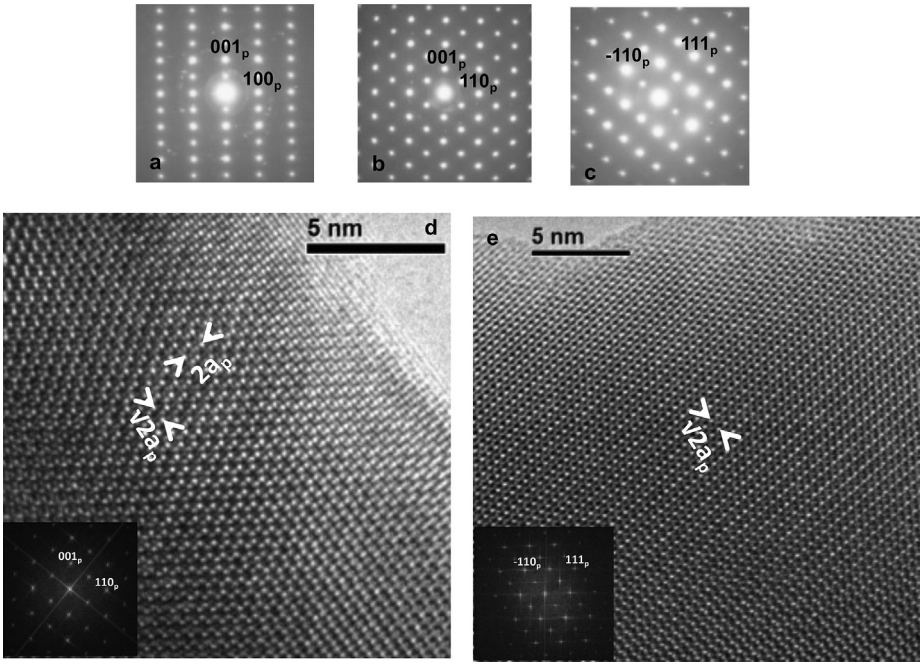

Fig. 4. SAED patterns of a $Nd_3Ni_2RuO_9$ crystal along the (a) $[001]_p$, (b) $[-110]_p$ and (c) $[11-1]_p$ zone axes; HRTEM images along the (d) $[-110]_p$ and (e) $[11-1]_p$ zone axes.

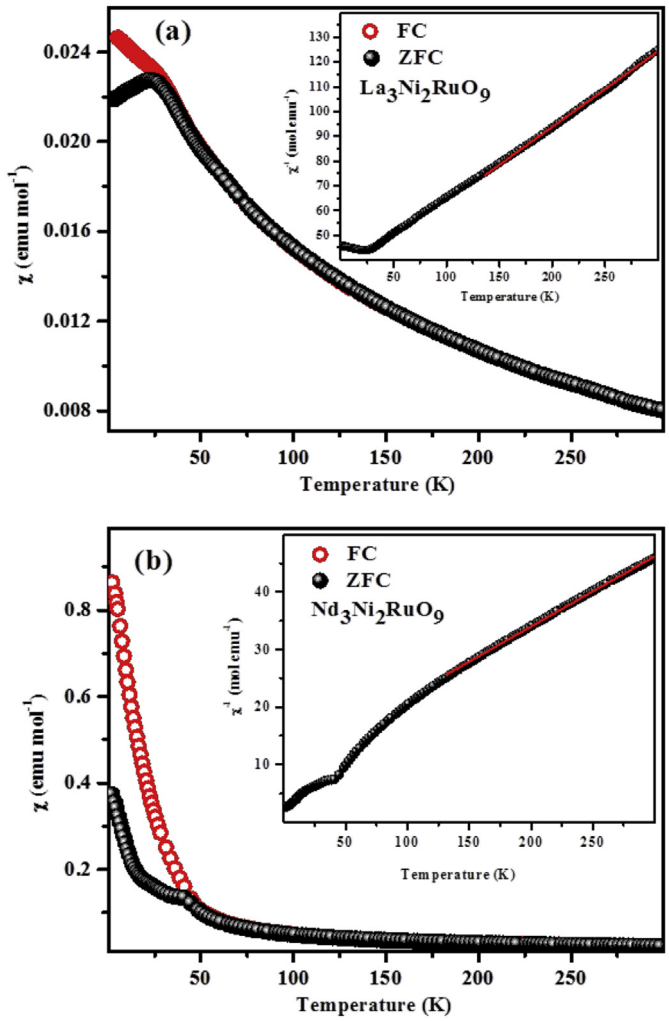

Fig. 5. Temperature dependence of the ZFC and FC molar magnetic susceptibility of a) $La_3Ni_2RuO_9$ and b) $Nd_3Ni_2RuO_9$.

3.2. Magnetic behavior

The temperature dependence of the magnetic molar susceptibility (χ) of $Ln_3Ni_2RuO_9$ oxides is plotted in Fig. 5. It can be seen that these oxides are paramagnetic above 100K, obeying a Curie-Weiss law ($\chi = C/(T-\theta)$) over a long temperature range. Table 2 summarizes the magnetic parameters obtained from their fit for both compounds. The experimental magnetic moments (μ_{exp}) agree with the expected values for Ni^{2+} (high spin), Ru^{5+} and Nd^{3+} oxidation states. In both oxides dominant antiferromagnetic interactions appear to be operative from the negative values of the Weiss constant (θ).

The χ *vs.* T data obtained under ZFC conditions show a maximum within the temperature range 25–35 K (see Fig. 5), suggesting an antiferromagnetic ordering. However, the divergence of ZFC and FC curves indicates a more complex behavior, where the cationic disorder within 2d sites and magnetic frustration could play an important role, as previously reported in some related perovskites [35–38].

The ZFC and FC magnetic susceptibilities remain coincident from room temperature down to T~35 K for the $La_3Ni_2RuO_9$ compound (Fig. 5(a)). Below that temperature, ZFC χ shows a maximum at 25 K while the FC data increase upon cooling down. However, as mentioned above, the neutron diffraction data obtained at 2 K (see Fig. 1(b)) reveals no magnetic contribution, evidenced through the absence of new reflections or the increase on the intensity of the nuclear peaks. These results demonstrate that no long-range antiferromagnetic order takes place in this compound and, therefore, the maximum observed at 25 K in the ZFC magnetic susceptibility measurements must be related to another magnetic phenomenon. Thus, the variations of the ac magnetic susceptibility (χ_{ac}) both with temperature and frequency (ω) were measured in order to determine the origin of that maximum. As it can be observed in Fig. 6 (top) χ′ measured with 0.5 Hz shows a maximum at 25 K (T_{max}). This maximum shifts to higher temperatures and decreases in magnitude with increasing excitation frequency. The shift, quantified by the expression $\Delta T_{max}\,[T_{max}\,\Delta(\log\omega)]^{-1}$, takes a value of ~0.033. Furthermore, this frequency-dependent maximum observed in χ′ is accompanied by a weak maximum in χ'', centred at lower temperatures and also frequency-dependent. These results are consistent with what is expected for insulating spin glasses [39].

Table 2
Theoretical (μ_{theor}) and experimental (μ_{exp}) magnetic moments, Weiss constant (θ) and freezing temperature (T_f) obtained for $Ln_3Ni_2RuO_9$ oxides (Ln = La and Nd).

Compound	μ_{theor} (μ_B)	μ_{exp} (μ_B)	Θ (K)	T_f (K)
$La_3Ni_2RuO_9$	5.57	5.30	- 106	25
$Nd_3Ni_2RuO_9$	8.37	8.40	- 81	35

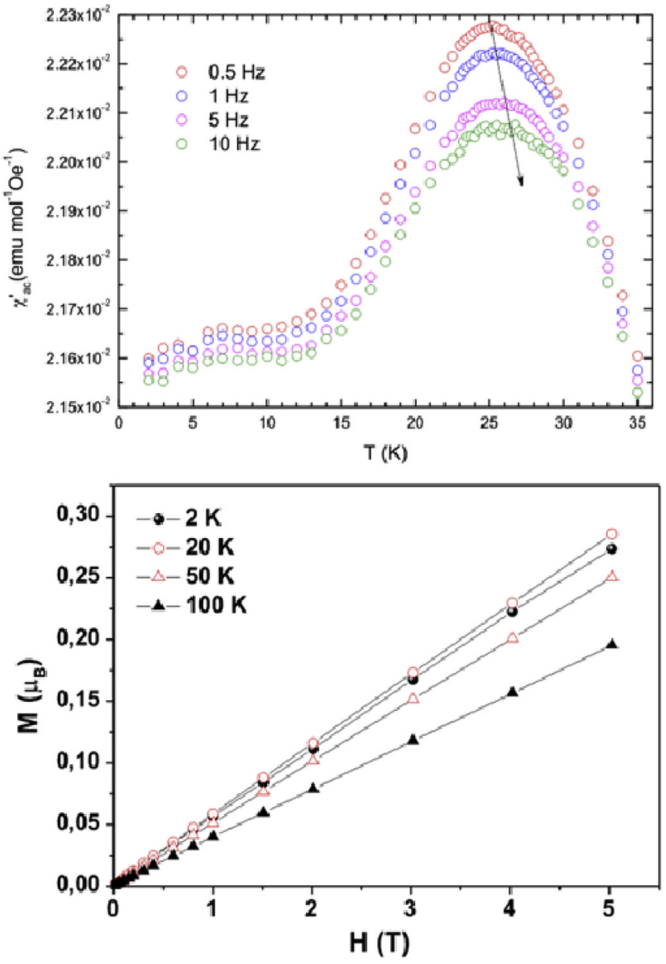

Fig. 6. Temperature variation of the χ'_{ac} at different frequencies (top) and M vs H plot (bottom) obtained at different temperatures for $La_3Ni_2RuO_9$.

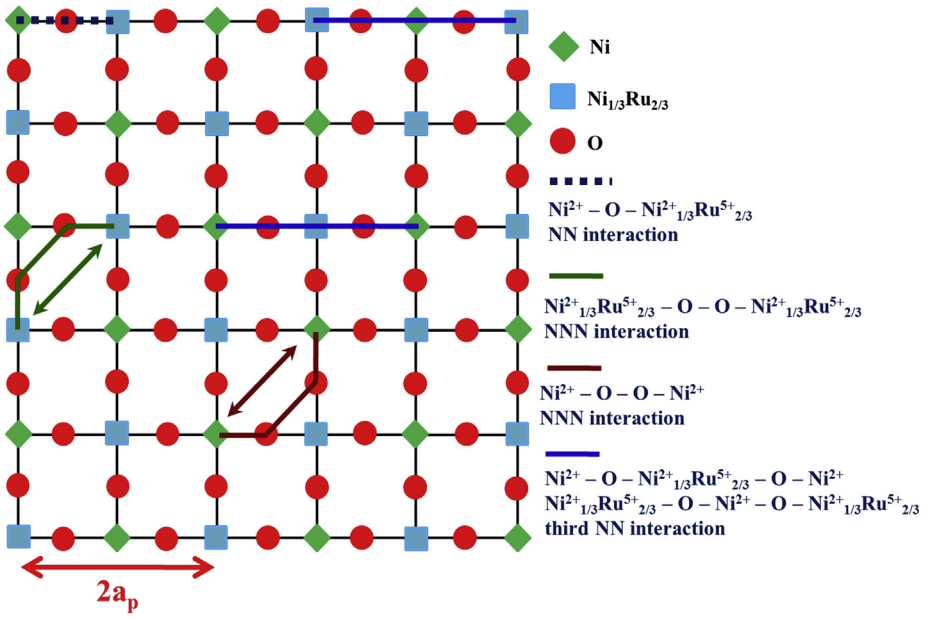

Fig. 7. Schematic representation showing the likely magnetic interactions in the idealized structure of $La_3Ni_2RuO_9$. NN interactions: Ni^{2+}–O–$Ni^{2+}{}_{1/3}Ru^{5+}{}_{2/3}$ (dotted blue line); NNN interactions: $Ni^{2+}{}_{1/3}Ru^{5+}{}_{2/3}$–O–O-$Ni^{2+}{}_{1/3}Ru^{5+}{}_{2/3}$ (continuous green line) and Ni^{2+}–O–O–Ni^{2+} (continuous brown line); third NN interactions: Ni^{2+}–O–$Ni^{2+}{}_{1/3}Ru^{5+}{}_{2/3}$–O–$Ni^{2+}$ and $Ni^{2+}{}_{1/3}Ru^{5+}{}_{2/3}$–O–$Ni^{2+}$–O–$Ni^{2+}{}_{1/3}Ru^{5+}{}_{2/3}$ (continuous blue line). (For interpretation of the references to colour in this figure legend, the reader is referred to the Web version of this article.)

This magnetic behavior of $La_3Ni_2RuO_9$ is different from that observed for the isostructural $La_3Ni_2SbO_9$ oxide, which develops ferrimagnetism below 105 K as result of the unbalanced spin-up and spin-down of the two types of Ni^{2+} ions located at the 2c and 2d sites in the crystal structure [17]. In this material, nearest neighbor (NN) antiferromagnetic Ni^{2+}–O–Ni^{2+} interactions accounted for such behavior (Fig. 7 and Fig. 8) and its net magnetization, which reaches 1.5 μ_B at 2K under a 4 T field, is located in domains but the magnetic order does not persist over distances long enough to be detected through neutron diffraction. Thus, $La_3Ni_2SbO_9$ oxide is considered as a relaxor-ferromagnet [17]. In contrast, $La_3Ni_2RuO_9$ shows linear dependence of isothermal dc-M with the magnetic field (see Fig. 6 (bottom)), and no hysteresis loop is observed. This feature suggests the absence of a spontaneous magnetization above or below T_{max}, so the antiferromagnetic interactions are mainly involved in the spin glass-like state. Therefore, the substitution of the diamagnetic Sb^{5+} for the paramagnetic Ru^{5+} induces dramatic changes in the magnetic behavior. Indeed, the presence of Ni^{2+} and Ru^{5+} in $La_3Ni_2RuO_9$ introduces different types of magnetic interactions, which are depicted in Fig. 7. If we consider the ferromagnetic Ni^{2+}– O – Ru^{5+} NN interaction [40], one would expect $La_3Ni_2RuO_9$ to be stronger ferromagnet than

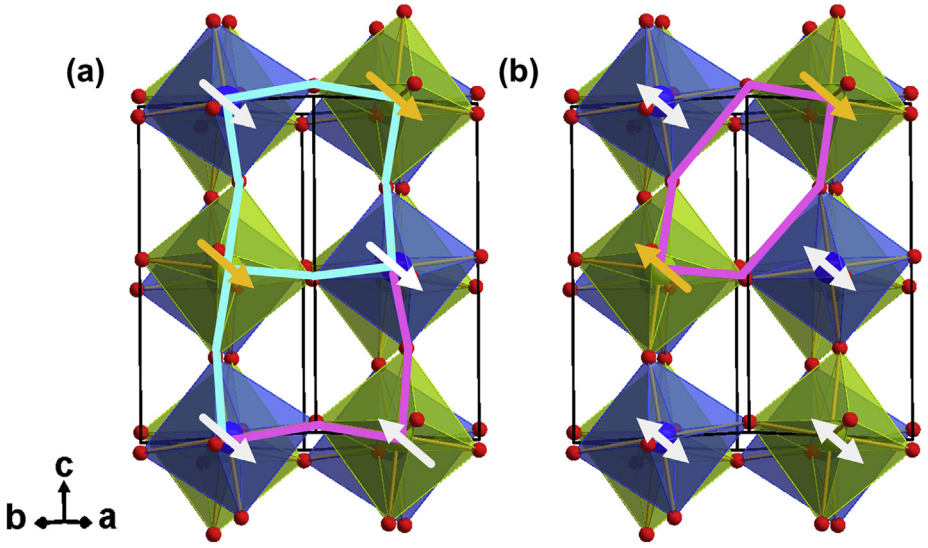

Fig. 8. Schematic diagrams showing the interaction pathways over the crystal structure of $Ln_3Ni_2RuO_9$ with the same colour code as that used in Fig. 3 (Ln atoms are deleted for clarity). White and orange arrows depict the magnetic moments of Ni^{2+} and Ru^{5+}, respectively. Cyan lines symbolize ferromagnetic interactions and pink lines stand for antiferromagnetic ones. a) NN interactions. b) Ru^{5+}–O–O–Ru^{5+} NNN interactions. The double headed arrows in b) represent the frustrated magnetic moments originated as a consequence of the dominant Ru^{5+}–O–O–Ru^{5+} NNN interactions, favoured by the more appropriated interaction angle, and the subsequent NN interactions Ni^{2+}–O–$Ru^{5+}$and Ni^{2+}–O–Ni^{2+}. (For interpretation of the references to colour in this figure legend, the reader is referred to the Web version of this article.)

$La_3Ni_2SbO_9$ (see Fig. 8(a)). However, the experimental results are different as $La_3Ni_2RuO_9$ is a disordered weak antiferromagnet (see Fig. 5), whose spins do not magnetically order even at 2K. The results clearly indicate a complex nature of the magnetic interactions between Ni^{2+} and Ru^{5+} in this oxide. It is relevant to note here that although the Ni^{2+}–O–Ru^{5+} NN interaction are weak ferromagnetic in the perovskite structure, theoretical calculations for $LaSrCuRuO_6$ perovskite point to the likely case of antiferromagnetic coupling of Cu^{2+} and Ru^{5+} [41,42]. However, the magnetic behavior found for $La_3Ni_2RuO_9$ is irreconcilable with any magnetic interaction considered for such cations.

The underlying reason for this apparent discrepancy between the predicted magnetic behavior based on the simple NN superexchange interactions and the experimental results lies on the presence of Ru^{5+}–O–O–Ru^{5+} next nearest neighbor (NNN) antiferromagnetic coupling as dominant interaction versus any other (a schematic representation of the interactions is depicted in Fig. 7). Indeed, Fig. 8(b) shows how magnetic frustration arises from such a scenario and therefore it is consistent with the spin-glass like behavior observed for $La_3Ni_2RuO_9$ at low temperatures. In this sense, theoretical considerations for $LaSrCuRuO_6$ perovskite have also shown that the Ru^{5+}–O–O–Ru^{5+} NNN antiferromagnetic coupling (90° interaction) becomes the dominant interaction. The deviation of Cu^{2+}–O–Ru^{5+} bond angle from the ideal 180° (around 155°), similar to that observed in $Ln_3Ni_2RuO_9$ oxides (see Table 1), as well as the presence of Ru^{5+} ions, seem to play an important role in weakening both the ~180° NN interactions and the Cu^{2+}–O–O–Cu^{2+} NNN interaction [41]. These results may be invoked to explain the weak antiferromagnetism with no long range ordering observed for $La_3Ni_2RuO_9$, where the Ni^{2+}–O–Ru^{5+} bond angles are in the range 148.3°–155.6°, giving rise to a frustrated ground state below 25 K.

The low temperature behavior of $Nd_3Ni_2RuO_9$ oxide is different from that of the lanthanum derivative. ZFC χ shows a maximum at 35 K, as it can be observed in Fig. 5(b). This maximum comes from the magnetic interactions within the Ni/Ru sublattices, similar to those described for the lanthanum compound. The PND pattern (see Fig. 2(b)), does not show magnetic peaks, indicating the absence of long range magnetic ordering down to 2K. The increase of the ZFC susceptibility below the maximum is due to the paramagnetic Nd^{3+} contribution, which remains magnetically independent without any kind of interaction with the Ni/Ru magnetic sublattices. Moreover, the downwards deviation observed in the Curie-Weiss behavior below 90K is mainly due to the crystal field effect on the splitting of the $^4I_{9/2}$ ground term of Nd^{3+} [43]. Below that temperature, this effect is partially masked by the interactions among the magnetic cations located at the B sites.

4. Conclusions

New perovskite-type $Ln_3Ni_2RuO_9$ (Ln = La, Nd) oxides were prepared by a metathesis reaction of the $Li_3Ni_2RuO_6$ oxide with LnOCl. The products crystallize in 1:1 double perovskite $A_2BB'O_6$ structure with monoclinic $P2_1/n$ symmetry, where the two octahedral B sites 2c and 2d are occupied by Ni^{2+} and ($Ni^{2+}_{1/3}Ru^{5+}_{2/3}$) cations respectively. Both oxides display a spin-glass like weak antiferromagnetism with no long-range magnetic order down to 2 K. The results are rationalized on the basis of the possible competing magnetic interactions between the octahedral-site transition metal atoms in the double perovskite structure.

Acknowledgements

J. G. thanks the National Academy of Sciences, Allahabad, India (NASI) for the award of Senior Scientist Fellowship. J. G. and S. N. thank the Department of Science and Technology (DST), Govt. Of India, for the award of an Indo-Spanish project. S. N. also thanks DST for a J C Bose Fellowship. The Spanish Ministery MINECO is also acknowledged for funding through projects. MAT2016-78362-C4-4R and MAT2017-84385-R respectively. Authors are also indebted with Professor M.A. Alario-Franco for useful discussion during this work.

Appendix A. Supplementary data

Supplementary data to this article can be found online at https://doi.org/10.1016/j.jallcom.2019.07.354.

References

[1] R.H. Mitchell, Perovskites: Modern and Ancient, Almaz Press Inc., Canada, 2002.
[2] M.T. Anderson, K.B. Greenwood, G.A. Taylor, K.R. Poeppelmeier, Prog. Solid State Chem. 22 (1993) 197–233.
[3] S. Vasala, M. Karppinen, Prog. Solid State Chem. 43 (2015) 1–36.
[4] K.-I. Kobayashi, T. Kimura, H. Sawada, K. Terakura, Y. Tokura, Nature 395 (1998) 677–680.
[5] N.S. Rogado, J. Li, A.W. Sleight, M.A. Subramanian, Adv. Mater. 17 (2005) 2225–2227.
[6] D.E. Cox, A.W. Sleight, Acta Crystallogr. B35 (1979) 1–10.
[7] A.W. Sleight, J.L. Gillson, P.E. Bierstedt, Solid State Commun. 17 (1975) 27–28.
[8] S. Chanda, S. Saha, A. Dutta, T.P. Sinha, Mater. Res. Bull. 62 (2015) 153–160.
[9] R.X. Silva, A.S. de Menezes, R.M. Almeida, R.L. Moreira, R. Paniago, X. Marti, H. Reichlova, M. Marysko, M.V. dos S. Rezende, C.W.A. Paschoal, J. Alloy. Comp. 661 (2016) 541–552.
[10] J. Krishna Murthy, A. Venimadhav, J. Alloy. Comp. 719 (2017) 341–346.
[11] J.P. Palakkal, C.R. Sankar, A.P. Paulose, M.R. Varma, J. Alloy. Comp. 743 (2018) 403–409.
[12] C. Zhang, W. Zhu, L. Yuan, H. Yuan, J. Alloy. Comp. 744 (2018) 395–403.
[13] J.P. Palakkala, C.R. Sankarb, A.P. Pauloseb, M. Valantc, A. Badasyanc, M.R. Varma, Mater. Res. Bull. 100 (2018) 226–233.
[14] R.C. Sahoo, S. Das, T.K. Nath, J. Magn. Magn. Mater. 460 (2018) 409–417.
[15] T.A. Vanderah, Science 298 (2002) 1182–1184.
[16] P.K. Davies, M.A. Akbas, J. Phys. Chem. Solids 61 (2000) 159–166.
[17] P.D. Battle, S.I. Evers, E.C. Hunter, M. Westwood, Inorg. Chem. 52 (2013) 6648–6653.
[18] E.C. Hunter, P.D. Battle, R.P. Sena, J. Hadermann, J. Solid State Chem. 248 (2017) 96–103.
[19] K. Dey, A. Indra, D. De, S. Majumdar, S. Giri, ACS Appl. Mater. Interfaces 8 (2016) 12901–12907.
[20] C.-M. Chin, P.D. Battle, S.J. Blundell, E. Hunter, F. Lang, M. Hendrickx, R.P. Sena, J. Hadermann, J. Solid State Chem. 258 (2018) 825–834.
[21] Y. Tang, E.C. Hunter, P.D. Battle, M. Hendrickx, J. Hadermann, J.M. Cadogan, Inorg. Chem. 57 (2018) 7438–7445.
[22] Y. Tang, E.C. Hunter, P.D. Battle, R.P. Sena, J. Hadermann, M. Avdeev, J.M. Cadogan, J. Solid State Chem. 242 (2016) 86–95.
[23] J. Bijelić, A. Stanković, B. Matasović, B. Marković, M. Bijelić, Ž. Skoko, J. Popović, G. Štefanić, Z. Jagličić, S. Zellmer, T. Preller, G. Garnweitner, T. Đorđević, P. Cop, B. Smarsly, I. Djerdj, CrystEngComm (2019), https://doi.org/10.1039/C8CE01483C.
[24] A. Chatterjee, S. Majumdar, S. Chatterjee, A.-C. Dippel, O. Gutowski, M.V. Zimmermann, S. Giri, J. Alloy. Comp. 778 (2019) 30–36.
[25] T.K. Mandal, J. Gopalakrishnan, J. Mater. Chem. 14 (2004) 1273–1280.
[26] T.K. Mandal, J. Gopalakrishnan, Chem. Mater. 17 (2005) 2310–2316.
[27] S. Laha, E. Morán, R. Sáez-Puche, M.A. Alario-Franco, A.J. Dos santos-García, E. Gonzalo, A. Kuhn, F. Garcia-Alvarado, T. Sivakumar, S. Tamilarasan, S. Natarajan, J. Gopalakrishnan, J. Solid State Chem. 203 (2013) 160–165.
[28] L.H. Brixner, E.P. Moore, Acta Crystallogr. C39 (1983) 1316.
[29] A.C. Larson, R.B. Von Dreele, General structure analysis system (GSAS), in: Los Alamos National Laboratory Report LAUR vol. 86, 2000.
[30] J. Rodriguez-Carvajal, Physica B 192 (1993) 55–69.
[31] W. Kraus, G. Nolze, J. Appl. Crystallogr. 29 (1996) 301–303.
[32] G.A. Bain, J.F. Berry, J. Chem. Educ. 85 (2008) 532–536.
[33] J.C. Pérez-Flores, D. Pérez-Coll, S. García-Martín, C. Ritter, G.C. Mather, J. Canales-Vázquez, M. Gálvez-Sánchez, F. García-Alvarado, U. Amador, Chem. Mater. 25 (2013) 2484–2494.
[34] M.S. Senn, W. Chen, T. Saito, S. García-Martín, J.P. Atffield, Y. Shimakawa, Chem. Mater. 26 (2014) 4832–4837.
[35] V. Primo-Martin, M. Jansen, J. Solid State Chem. 157 (2001) 76–85.
[36] P.D. Battle, T.C. Gibb, C.W. Jones, F. Studer, J. Solid State Chem. 78 (1989) 281–293.
[37] T. Stoyanova-Lyubenova, A.J. Dos Santos-García, E. Urones-Garrote, M.J. Torralvo, M.A. Alario-Franco, Dalton Trans. 43 (2014) 1117–1124.
[38] J. Xiong, J. Yan, A.A. Aczel, P.M. Woodward, J. Solid State Chem. 258 (2018) 762–767.

[39] K. Moorjani, J.M.D. Coey, Magnetic Glasses, Elsevier Amsterdam, 1984, p. 36.
[40] J.B. Goodenough, Magnetism and the Chemical Bond, Interscience monographs on chemistry, 1963.
[41] S.H. Kim, P.D. Battle, J. Magn. Magn. Mater. 123 (1993) 273–282.
[42] P.A. Kumar, R. Mathieu, R. Vijayaraghavan, S. Majumdar, O. Karis, P. Nordblad, B. Sanyal, O. Eriksson, D.D. Sarma, Phys. Rev. B 86 (2012), 094421.
[43] F. Fernández, R. Sáez-Puche, C. Cascales, C.M. Marcano, I. Rasines, J. Phys. Chem. Solids 50 (1989) 871–875.